

Graphene-assisted critically-coupled optical ring modulator

Michele Midrio,^{1,*} Stefano Boscolo,¹ Michele Moresco,²
Marco Romagnoli,² Costantino De Angelis,³ Andrea Locatelli,³
and Antonio-Daniele Capobianco⁴

¹*Dipartimento di Ingegneria Elettrica Gestionale e Meccanica,
Università degli Studi di Udine, 33100 Udine, Italy*

²*PhotonIC Corporation, 5800 Uplander Way, Los Angeles, CA 90230, USA
Massachusetts Institute of Technology, 77 Massachusetts Ave, Cambridge, MA 02139, USA*

³*Dipartimento di Ingegneria dell'Informazione,
Università degli Studi di Brescia, 25123 Brescia, Italy*

⁴*Dipartimento di Ingegneria dell'Informazione,
Università degli Studi di Padova, 35131 Padova, Italy*

[*midrio@uniud.it](mailto:midrio@uniud.it)

Abstract: Graphene's conductivity at optical frequencies can be varied upon injection of carriers. In the present paper, this effect is used to modulate losses of an optical wave traveling inside a ring cavity. This way an optical modulator based on the critical-coupling concept first introduced by Yariv can be realized. Through numerical simulations, we show that a modulator featuring a bandwidth as large as 100 GHz can be designed with switching energy in the order of few fJ per bit. Also, we show that operations with driving voltages below 1.2 volt could be obtained, thus making the proposed modulator compatible with requirements of low-voltage CMOS technology.

© 2012 Optical Society of America

OCIS codes: (250.4110) Modulators; (250.3140) Integrated optoelectronic circuits; (160.3130) Integrated optics materials; (060.4510) Optical communications.

References and links

1. A. Yariv, "Critical coupling and its control in optical waveguide-ring resonator systems," *IEEE Photon. Technol. Lett.* **14**, 483–485 (2002).
2. R. A. Soref, and B. R. Bennett, "Kramers-Kronig analysis of electro-optical switching in silicon," *Proc. SPIE* **704**, 32–37 (1987).
3. J. P. Lorenzo and R. A. Soref, "1.3 μm electro-optic silicon switch," *J. Appl. Phys.* **51**, 6–8 (1987).
4. L. Friedman, R. A. Soref, and J. P. Lorenzo, "Silicon double-injection electro-optic modulator with junction gate control," *J. Appl. Phys.* **63**, 1831–1839 (1988).
5. S. R. Giguere, L. Friedman, R. A. Soref, and J. P. Lorenzo, "Simulation studies of silicon electro-optic waveguide devices," *J. Appl. Phys.* **68**, 4964–4970 (1990).
6. G. V. Treyez, P. G. May, and J. M. Halbout, "Silicon optical modulators at 1.3 micrometer based on free-carrier absorption," *IEEE Electron. Dev. Lett.* **12**, 276–278 (1991).
7. G. V. Treyez, P. G. May, and J. M. Halbout, "Silicon Mach-Zehnder waveguide interferometers based on the plasma dispersion effect," *Appl. Phys. Lett.* **59**, 771–773 (1991).
8. U. Fischer, B. Schuppert, and K. Petermann, "Integrated optical switches in silicon based on SiGe-waveguides," *IEEE Photon. Technol. Lett.* **5**, 785–787 (1993).
9. H. C. Huang and T. C. Lo, "Simulation and analysis of silicon electro-optic modulators utilizing the carrier-dispersion effect and impact-ionization mechanism," *J. Appl. Phys.* **74**, 1521–1582 (1993).
10. A. Cutolo, M. Iodice, P. Spirito, and L. Zeni, "Silicon electro-optic modulator based on a three-terminal device integrated in a low-loss single-mode SOI waveguide," *J. Lightwave Technol.* **15**, 505–518 (1997).

11. A. Sciuto, S. Libertino, A. Alessandria, S. Coffa, and G. Coppola, "Design, fabrication and testing of an integrated Si-based light modulator," *J. Lightwave Technol.* **21**, 228–235 (2003).
12. C. A. Barrios, V. R. de Almeida, and M. Lipson, "Low-power-consumption short-length and high-modulation-depth silicon electrooptic modulator," *J. Lightwave Technol.* **21**, 1089–1098 (2003).
13. A. Liu, R. Jones, L. Liao, D. Samara-Rubio, D. Rubin, O. Cohen, R. Nicolaescu, and M. Paniccia, "A high-speed silicon optical modulator based on a metal-oxide semiconductor capacitor," *Nature* **427**, 615–618 (2004).
14. A. Liu, L. Liao, D. Rubin, H. Nguyen, B. Ciftcioglu, Y. Chetrit, N. Izhaki, and M. Paniccia, "High-speed optical modulation based on carrier depletion in a silicon waveguide," *Opt. Express* **15**, 660–668 (2007).
15. Q. Xu, S. Manipatrumi, B. Schmidt, J. Shakya, and M. Lipson, "12.5 Gbit/s carrier-injection-based silicon microring silicon modulators," *Opt. Express* **15**, 430–436 (2007).
16. Q. Xu, D. Fattal, and R. G. Beausoleil, "Silicon microring resonators with 1.5- μm radius," *Opt. Express* **16**, 4309–4315 (2008).
17. P. Dong, R. Shafiiha, S. Liao, H. Liang, N.-N. Feng, D. Feng, G. Li, X. Zheng, A. V. Krishnamoorthy, and M. Ashgari, "Wavelength-tunable silicon microring modulator," *Opt. Express* **18**, 10941–10946 (2010).
18. W. A. Zortman, M. R. Watts, D. C. Trotter, R. W. Young and A. L. Lentine, "Low-power high-speed silicon microdisk modulators," in *Proc. Conference on Lasers and Electro-Optics/Quantum Electronics and Laser Science Conference (CLEO/QELS)* (San Jose, Calif., 2004), paper CThJ4.
19. M. R. Watts, D. C. Trotter, R. W. Young, and A. L. Lentine, "Ultralow power silicon microdisk modulators and switches," in *Proc. of the 5th IEEE International Conference on Group IV Photonics* (Cardiff, Wales, 2008).
20. M. Liu, X. Yin, E. Ulin-Avila, B. Geng, T. Zentgraf, L. Ju, F. Wang, and X. Zhang, "A graphene-based broadband optical modulator," *Nature* **474**, 64–67 (2011).
21. M. Liu, X. Yin, and X. Zhang, "Double-layer graphene optical modulator," *Nano Lett.* **12**, 1482–1485 (2012).
22. A. K. Geim and K. S. Novoselov, "The rise of graphene," *Nat. Mater.* **6**, 183–191 (2007).
23. T. Stauber, N. M. R. Peres, and A. K. Geim, "Optical conductivity of graphene in the visible region of the spectrum," *Phys. Rev. B* **78**, 085432 (2008).
24. A. Vakil and N. Engheta, "Transformation optics using graphene," *Science* **332**, 1291–1294 (2008).
25. G. W. Hanson, "Dyadic Green's function and guided surface waves for a surface conductivity model of graphene," *J. Appl. Phys.* **103**, 064302 (2008).
26. CST Microwave Studio 2012. Darmstadt, Germany.
27. T. Barwicz and H. A. Haus, "Three-dimensional analysis of scattering losses due to sidewall roughness in microphotonic waveguides," *J. Lightwave Technol.* **23**, 2719–2732 (2005).
28. K. K. Lee, D. R. Lim, L. C. Kimerling, J. Shin, and F. Cerrina, "Fabrication of ultralow-loss Si/SiO₂ waveguides by roughness reduction," *Opt. Lett.* **23**, 1888–1890 (2001).
29. M. Moresco, M. Romagnoli, S. Boscolo, and M. Midrio, "Method for Characterization of Si waveguide propagation loss," submitted to *Opt. Express* (2012).
30. A. A. Balandin, S. Ghosh, W. Bao, I. Calizo, D. Teweldebrhan, F. Miao, and C. N. Lau, "Superior thermal conductivity of single-layer graphene," *Nano Lett.* **8**, 902–907 (2008).
31. C. T. DeRose, M. R. Watts, D. C. Trotter, D. L. Luck, G. N. Nielson, and R. W. Young, "Silicon microring modulator with integrated heater and temperature sensor for thermal control," in *Lasers and Electro-Optics/Quantum Electronics and Laser Science Conference 2010*, paper CThJ3.

1. Introduction

Optical modulators are key components for telecommunications and optical interconnections. They are among the first integrated optics devices that have been studied since the mid 1980s.

Earliest designs were based on ferroelectric materials or III-V compounds. However, the dominance of silicon as the semiconductor choice for electronics, and the need of integration of optical and electronic functionalities onto the same chip eventually shifted the research efforts towards structures based on silicon-on-insulator substrates. A list of contributions that cover some relevant steps toward the design of modern modulators can be found in refs. [1–14].

Most of the structures reported in the papers above essentially are straight waveguides in a Mach-Zehnder configuration. The key physical mechanism they rely on is the *plasma dispersion effect*: silicon losses are modified upon injection of free carriers. Through Kramers-Kronig relations, the refractive index of the material is modified as well. This may be used to produce a π -shift in one of the Mach-Zehnder arms, and finally obtain the desired intensity modulation. The major drawback of this scheme is in the relative large dimensions it requires. Indeed, as plasma-dispersion can only induce small variations of the refractive index, interaction lengths in the range of hundreds of microns to millimeters are needed.

In an attempt to reduce dimensions, and therefore allow for greater integration, ring-modulators were successively proposed. Plasma dispersion effect still is the key physical mechanism. However, light which travels inside a cavity may now experience the refractive index change for thousands of time. This way, even a very tiny variation of the propagation constant may shift the wavelength of resonance by an amount large enough to allow for efficient amplitude modulation.

Based on this idea, devices with footprints in the range of 10 squared microns have been demonstrated [15–17]. Owing to these very small dimensions, these devices also proved to have exceptional performance in terms of power consumption [18, 19]. The price to pay is the narrow bandwidth that resonances can offer. These are often limited to few GHz, and this finally brings to the need for stringent fabrication capabilities and thermal control.

More recently, a novel kind of modulator has appeared in the open literature [20, 21]. It might represent a real break-through in the integrated-optics scenario, as it differs from plasma-dispersion-effect modulators in two respects.

1. The first is the use of *graphene*, the single sheet of carbon atoms in a hexagonal lattice that, among many other exceptional properties, has a much higher electron mobility than silicon [22].
2. The second is the operation principle it exploits. Indeed, this modulator directly relies on loss modulation rather than on loss-induced refractive index variations. The striking point is that, essentially, this is “just” an electro-absorption modulator. As such, it may operate over a virtually endless optical band, but with much better performance than “conventional” electro-optic modulators in terms of electrical bandwidth.

Unfortunately, the differential loss that can be achieved by modulating graphene losses is relatively small. Values in the range of 0.1÷0.15 dB/μm were demonstrated in refs. [20, 21]. This in turn means that if an extinction ratio of 6÷10 dB is looked for between the “ON” and “OFF” states of the modulator, a device length in the order of 50÷100 μm must be foreseen. As we shall illustrate below this could lead to rather severe impairments in terms of switching-energy consumption.

At this stage, one might observe that it looks like the potential of graphene in the framework of optical modulation were following the same path as that of the plasma-dispersion-effect. Indeed, a promising technology has become available, but dimensions (and energy consumption) yet are the main limiting factors. Just in the same way as it was done with plasma-dispersion-effect modulators, one might therefore wonder whether inserting graphene into a resonant ring structure could help to improve the performance or not. The aim of the present paper is that of investigating the point, to quantify the bandwidth and energy consumption that can be foreseen when designing a graphene-assisted optical ring modulator.

2. Principle of operation

We exploit the physical effect introduced in 2002 by A. Yariv: the critical coupling [1] that can be obtained in ring structure as the one sketched in the inset of Fig. 1.

For the sake of clarity we briefly review the main result of ref. [1], and we use the same symbols as in the original paper. Letting t and α the single-pass transmission through the straight waveguide, and through the ring, respectively, the scattering matrix of the coupler reads as

$$\begin{bmatrix} b_1 \\ b_2 \end{bmatrix} = \begin{bmatrix} t & k^* \\ -k & t \end{bmatrix} \begin{bmatrix} a_1 \\ a_2 \end{bmatrix}, \quad \text{with} \quad |t|^2 + |k|^2 = 1 \quad \text{and} \quad a_2 = \alpha b_2 e^{i\varphi} \quad . \quad (1)$$

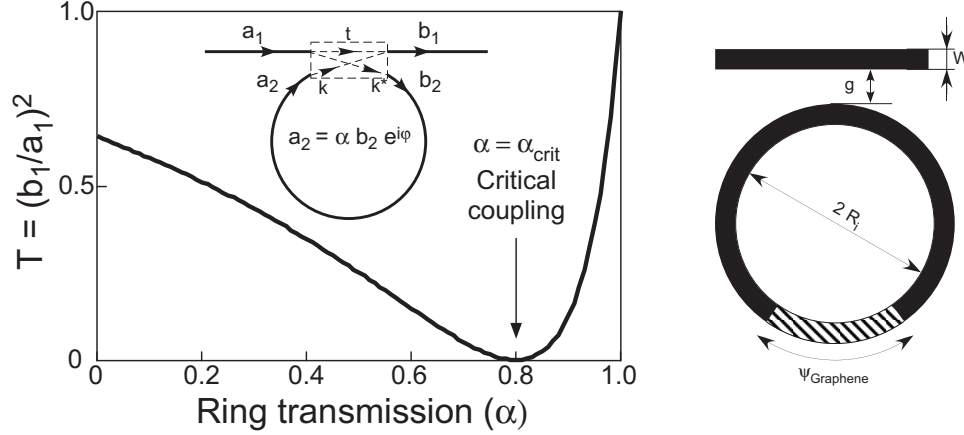


Fig. 1. Left: transmission curve as a function of the ring transmission α for $t=0.8$ at resonance. Inset: schematic diagram of the ring structure, with definition of the straight waveguide and ring single pass transmission, t and α , respectively. Right: the layout of the graphene-assisted optical ring modulator we have used in our simulations. The dashed area is the region where graphene is present.

At resonance ($\varphi = m 2\pi$), the transmitted power is

$$T = \left| \frac{b_1}{a_1} \right|^2 = \frac{(\alpha - |t|)^2}{(1 - \alpha|t|)^2} \quad (2)$$

When $\alpha \equiv \alpha_{\text{crit}} = t$ no power is transmitted; whereas, when $\alpha \rightarrow 1$, almost unitary transmission is obtained (at the wavelength of resonance). At this stage, we quote an observation made by Yariv in his paper: “If we can learn how to control α and/or t , we have a basis for a switching technology. If we can do it sufficiently rapid, we have the basis of a new type of an optical modulator”. As it has been shown by Liu *et al.* in [20], rapid control of α is precisely what one can do with graphene, and this is the operation principle we want to investigate.

Let us indeed consider the left part of Fig. 1, where the transmission curve of Eq. (2) is shown for $t = 0.8$. Observe that for $\alpha > \alpha_{\text{crit}} = t$ the transmission rapidly raises from zero towards one. The closer is α_{crit} to 1, the steeper is the raise of the curve on the right hand side of the critical coupling point.

On the basis of this simple fact, the design of the modulator is easy. Consider the right panel of Fig. 1 and assume that a given gap distance g has been chosen. Initially, set the graphene’s conductivity high (the exact values of conductivity that can realistically be obtained at optical frequencies will be clarified in the next section). By acting on of the dimensions of the graphene region (i.e. on the angle ψ_{Graphene} in the figure) we may tune the ring losses and drive the ring at its critical condition. When this is done, no light is transmitted to the output port.

If now the graphene’s conductivity is switched low, only curvature and/or scattering losses remain in the ring. If these are small enough, the overall single-pass ring transmission $\alpha \rightarrow 1$. This way, one moves to the right side of the critical coupling point of Fig. 1 and almost lossless transmission is obtained (at resonance).

This is, essentially, the procedure that we have followed to design the device with the help of numerical simulations we describe below.

2.1. Waveguide and ring geometry

As schematically described in Fig. 2, throughout the whole set of simulations we performed, the bus and ring waveguides were supposed to be constituted by a $W = 400$ nm silicon core with relative dielectric constant equal to 12.1. The height of both the bus and ring waveguides were set equal to 220 nm. A first layer of graphene, with thickness $h_{\text{Graphene}} = 0.34$ nm was placed directly over the core (in the region where it is present, namely in the dashed zone of Fig. 1). Next, a coating layer of alumina was placed on top of both graphene and silicon. The relative dielectric constant of alumina was assumed to be equal to 3 at optical frequencies, and to 10 at microwave frequencies (this value will be used below to estimate the energy required for switching). Alumina was assumed to form a planar surface, as it would occur if a planarization process including, for instance, chemical mechanical polishing had been used. This way, the thickness of the alumina layer was $h_{\text{Alumina}} + h_{\text{Graphene}} = 7.34$ nm over the waveguide core, and $h_{\text{Alumina}} = 7$ nm over graphene. A second layer of graphene, with the same thickness and angular extension ψ_{Graphene} was placed next on top of the alumina coating. Finally, silica with relative dielectric constant equal to 2.25 was assumed to surround the whole structure. The fundamental quasi-TE mode was used to feed the structure in all the simulations.

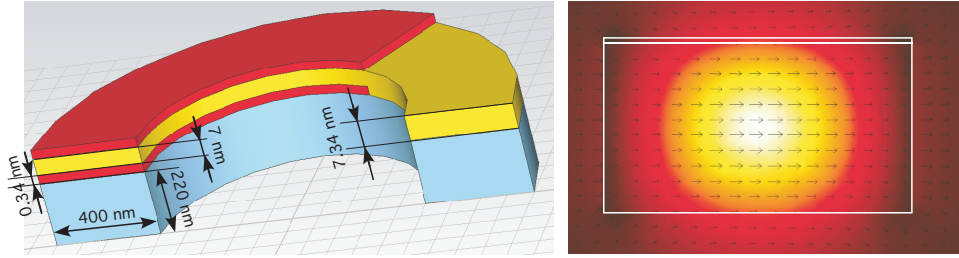


Fig. 2. Left panel: Schematic diagram (not to scale) of the ring waveguide. Light blue is the silicon core, yellow is alumina and red is graphene, respectively. Silica cladding is not shown. Right panel: Power density and lines of force of the electric field of the fundamental TE mode.

3. On the conductivity of graphene at optical frequencies

Before entering into the details of the numerical simulations, we recall some basic facts concerning the values that graphene's conductivity can attain at optical frequencies. To this end, we use a result derived in ref. [23], which gives the following dependence of the real part of the conductivity on frequency (ω), temperature (T) and chemical potential (μ_C):

$$\sigma_R(\omega) \simeq \frac{\sigma_0}{2} \left(\tanh \frac{\hbar\omega + 2\mu_C}{4k_B T} + \tanh \frac{\hbar\omega - 2\mu_C}{4k_B T} \right). \quad (3)$$

Here \hbar and k_B are the reduced Planck's and Boltzmann constants, respectively, and

$$\sigma_0 = \frac{e^2}{4\hbar} \simeq 6.0853 \times 10^{-5} \text{ Siemens} \quad (4)$$

with e the electron charge.

A plot of Eq. (3) is reported in the left panel of Fig. 3 for $T=300$ K and chemical potential μ_C equal to 0.3 and 0.5 eV with solid and dashed lines, respectively. The vertical line at 0.8 eV shows the conductivity for photons having free-space wavelength in the vicinity of 1550 nm. Observe that at these wavelengths, a modest shift of the chemical potential from 0.3 to 0.5

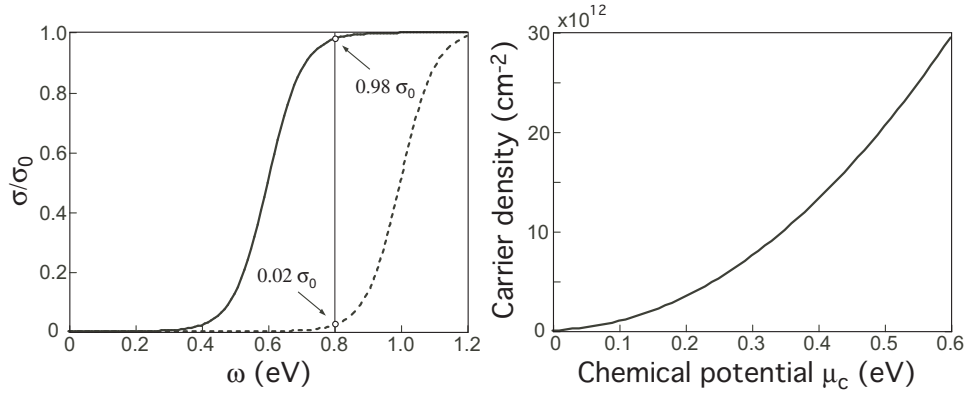


Fig. 3. Left panel: Conductivity of graphene for chemical potential $\mu_C = 0.3$ eV (solid line) and $\mu_C = 0.5$ eV (dashed line) for $T=300$ K. The vertical line highlights value of the conductivity for photons with free-space wavelength equal to 1550 nm. Right panel: relation between carrier density and chemical potential for an isolated sheet of graphene.

eV allows to span the conductivity from $0.02 \sigma_0$ to $0.98 \sigma_0$, i.e. over the almost entire range of values it may attain. A decrease of the chemical potential below 0.3 eV shifts the curve towards the left side, eventually yielding an almost constant value of conductivity $\sigma = \sigma_0$ for wavelengths around 1550 nm. This in turn means that the device should be operated by applying a bias-voltage to reach the 0.3 eV chemical potential, and switching between high and low conductivities can successively be performed with a 0.2 eV increase of the chemical potential.

Also observe that Eq. (3) gives a bulk conductivity with the dimensions of Siemens. Whereas, in our simulations, graphene is modeled as a brick with a finite thickness ($h_{\text{Graphene}} = 0.34$ nm), which needs to be assigned a Siemens/meter conductivity. Therefore, following the method used in ref. [24], when we want to simulate highly or poorly conductive graphene, we set the values as follows:

$$\sigma_{\text{High}} = \frac{0.98 \sigma_0}{h_{\text{Graphene}}} \simeq 1.75 \times 10^5 \text{ S/m} \quad , \quad \sigma_{\text{Low}} = \frac{0.02 \sigma_0}{h_{\text{Graphene}}} \simeq 3.58 \times 10^3 \text{ S/m} \quad .$$

With the same procedure, we also evaluated the relative dielectric constant of graphene in both the low and high conductivity states. Using the expression for the complex interband conductivity of ref. [25], we found that for the high and low conductivity cases $\epsilon_{\text{High}} \simeq 10.44$ and $\epsilon_{\text{Low}} \simeq 11.91$, respectively. Notice that, as we will show below, given the very reduced thickness of graphene, a change in the value of the dielectric constant of graphene has a very minor effect on the propagation constant of the traveling mode.

We close the present section by also giving an estimate of the carrier densities (n_s) needed to reach the above values of chemical potentials. These densities will be needed later to evaluate the energy required for switching. To this end we recall that, at least for an isolated sheet of graphene, Hanson has derived the following relation between the chemical potential and the carrier density [25]

$$n_s = \frac{2}{\pi \hbar^2 v_F^2} \int_0^{+\infty} \epsilon [f_d(\epsilon) - f_d(\epsilon + 2\mu_C)] d\epsilon \quad , \quad (5)$$

where $f_d(\epsilon) = \left(e^{(\epsilon - \mu_C)/k_B T} + 1 \right)^{-1}$ is the Fermi-Dirac distribution and $v_F \simeq 9.5 \times 10^5$ m/s is the Fermi velocity. A plot of Eq. (5) is shown in the right panel of Fig. 3. It is observed that

chemical potentials equal to 0.3 and 0.5 eV can be obtained with carrier densities roughly equal to $\rho_{\text{OFF}} = 7.5 \times 10^{12} \text{ cm}^{-2}$ and $\rho_{\text{ON}} = 20.5 \times 10^{12} \text{ cm}^{-2}$, respectively. Use of subscripts OFF and ON will become clear later on.

4. Numerical simulations and results

We refer again to the structure illustrated in the right panel of Fig. 1 above. All our simulations were performed with commercial codes CST [26] and COMSOL. Frequency-domain simulations based on the finite-element method were performed with both the codes. CST was used to perform all the simulations of propagation through the ring. Whereas, COMSOL was used mainly to check the accuracy of the propagation constant and mode profile computed by the modal analysis tool of CST. We underline that use of an accurate tetrahedral unstructured mesh proved to be compulsory in order to get reliable results. This is consistent with results of ref. [27] where it was shown that even a 2 nm roughness in the waveguide sidewalls may give rise to remarkable scattering losses. This in turn means that if we had used a structured staircase mesh, even with cell dimensions as small as 10 nm, a value which would have brought to extreme large computational time and memory occupancy, the main numerical effect we had observed would have been that of an artificially big scattering loss.

A preliminary analysis was conducted to characterize the propagation constant of the mode in the waveguide (a straight one), either in the absence or in the presence of graphene, both in the high and low conductivity states.

It turned out that, for free space-wavelength $\lambda_0 \simeq 1550 \text{ nm}$, the mode has the following effective indices:

No graphene	$n_{\text{eff}} = 2.2576$
Graphene with low conductivity ($\sigma = \sigma_{\text{Low}}, \epsilon = \epsilon_{\text{Low}}$)	$n_{\text{eff}} = 2.2543 - i8.42 \times 10^{-5}$
Graphene with high conductivity ($\sigma = \sigma_{\text{High}}, \epsilon = \epsilon_{\text{High}}$)	$n_{\text{eff}} = 2.2546 - i3.79 \times 10^{-3}$

It is observed that graphene's effect is mostly on the imaginary part of the effective index, i.e. on losses. Indeed the mode profiles in the three cases above were almost undistinguishable. This in turn means that no scattering from mode-mismatch is expected when the field crosses the interfaces between the ring sections with and without graphene. Indeed, both because of its extremely tiny thickness, and of relatively small conductivity, graphene acts as a sort of first-order perturbative term: mainly, it introduces an imaginary part in the propagation constant without altering the mode profile in a significant way.

A second preliminary analysis was also conducted in order to evaluate the bending losses as a function of radius of curvature. The results of this analysis are reported in Fig. 4 for rings in the absence (solid line) and presence (dashed line) of graphene, respectively. In these simulations, the conductivity of graphene, when present, is set equal to σ_{High} . The abscissa in the figure has to be intended as the average ring radius (i.e. the internal ring radius plus half the ring waveguide width).

In the absence of graphene, the bending losses decrease towards zero for increasing radii, as expected. Whereas, the behavior in the presence of graphene is more interesting. For large radii, the curve tends to a limiting value, in the order of $0.13 \text{ dB}/\mu\text{m}$. This value exactly corresponds to the loss of the mode in the straight waveguide we have discussed above, when we found the effective index $n_{\text{eff}} = 2.2546 - i3.79 \times 10^{-3}$. We conclude that the curvature loss is negligible with respect to graphene absorption for curvature radii greater than about $3 \mu\text{m}$. For smaller radii, bending losses tend to become so large that they shadow graphene's absorption.

Since the critical coupling is the key factor in the proposed device, and since this strongly depends on ring losses, we conclude the presentation of these preliminary results by stressing

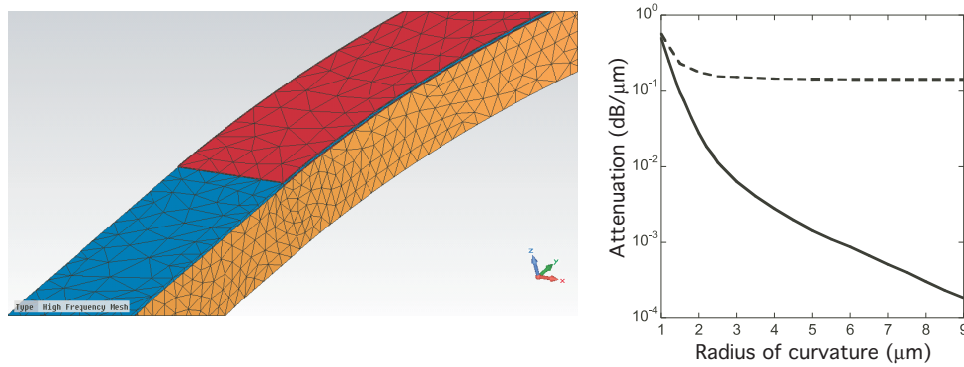


Fig. 4. Left panel: a plot from CST main window, showing the structure used in the simulation performed to compute bending losses along with the mesh. The orange, blue and red regions are the silicon core, alumina coating and graphene layers, respectively. Though barely observable, two layers of graphene are present. Right panel: bending loss in the absence and presence of the two graphene layers (solid and dashed lines, respectively). The graphene conductivity is set equal to σ_{High} .

one more time the issue of scattering. We recall that we used a very fine tetrahedral mesh throughout the whole set of our simulations (see the left panel of Fig. 4 for an example of such mesh). This way, we removed the roughness of sidewalls, eventually nulling any scattering loss. One might wonder whether this is a too ideal case, so that our numerical result will not fit a real experiment. Actually, we remark that in a real device the losses due to scattering are in the order of 2×10^{-4} dB/ μm or less [27–29]. Therefore, if we look at the solid curve in Fig. 4 we see that scattering losses can be neglected with respect to bending losses as long as the radius of curvature is smaller than $9 \mu\text{m}$. Since in all the simulations we performed the average ring radius was set equal to $r = 5 \mu\text{m}$, we conclude that having numerically nulled the scattering losses is not a limit of our simulations indeed.

We finally come to the details of the numerical simulations we performed to design the graphene-assisted critically-coupled ring resonator. With the graphene in the high-conductivity state, we varied the gap values from 80 to 160 nm at steps of 10 nm. For each value of gap, we evaluated the ring transmission when we also varied the extension of the graphene region through the angle ψ_{Graphene} (see Fig. 1). The ring transmission swept from over to under-coupling conditions for increasing ψ_{Graphene} . The critical-coupling could be easily determined by finding the transmission minimum vs. ψ_{Graphene} . For instance, it turned out that when the gap $g = 100$ nm, the critical coupling was reached for $\psi_{\text{Graphene}} = 116$ degrees. As it is shown by the solid line in the left panel of Fig. 5, for such a case the transmission dropped to almost -45 dB at the resonance frequency of 193.66 THz (corresponding to the free-space wavelength $\lambda_0 \simeq 1550$ nm).

An estimate of losses in the ring is useful at this stage. Roughly, it is given by the sum of loss due to graphene absorption (in the region where the graphene is present) plus loss due to bending in the rest of the ring. This accounts to

$$A_{\text{High}} \simeq 0.13 \text{ dB}/\mu\text{m} \cdot L_{\text{Graphene}} + 1.4 \times 10^{-3} \text{ dB}/\mu\text{m} (L_{\text{Ring}} - L_{\text{Graphene}}) \simeq 1.34 \text{ dB} \quad , \quad (6)$$

where we used $L_{\text{Ring}} = 10\pi \mu\text{m}$, $L_{\text{Graphene}} = 116/360 L_{\text{Ring}}$, and we took the value of bending losses for the $5 \mu\text{m}$ average radius from Fig. 4. In linear scale, this value would correspond to a single-pass ring loss $\alpha = \alpha_{\text{crit}} \simeq 0.73$ in Eq. (2). Recall that at the critical condition, also $t = \alpha_{\text{crit}}$.

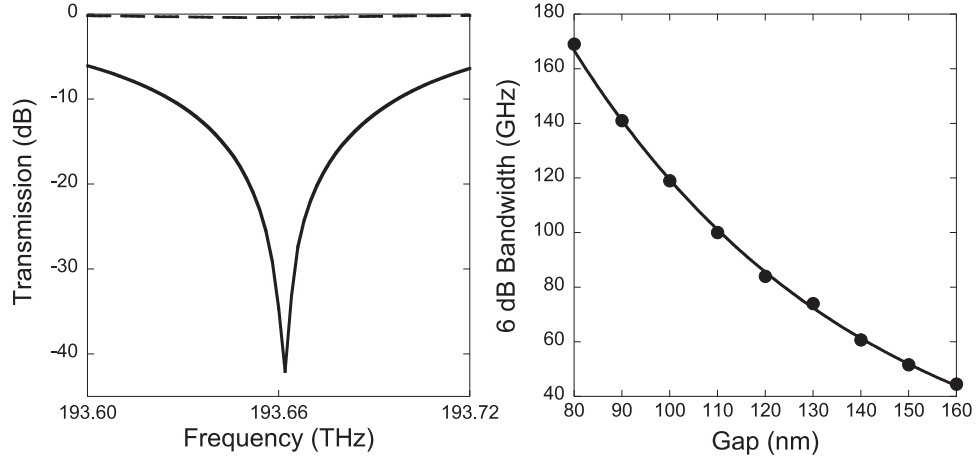


Fig. 5. Left panel: Transmission in a critically-coupled ring with gap $g = 100$ nm, average radius equal to $5 \mu\text{m}$ for graphene conductivity $\sigma = \sigma_{\text{High}}$ (solid line) and $\sigma = \sigma_{\text{Low}}$ (dashed curve). Right panel: numerically computed 6 dB bandwidth versus the gap distance g .

If the graphene's conductivity is switched to the low state, the ring loss changes due to the reduced graphene absorption. Indeed, we have seen above that the effective index of the mode which travels in a waveguide coated by graphene with $\sigma = \sigma_{\text{Low}}$ is $n_{\text{eff}} = 2.2543 - i8.42 \times 10^{-5}$, corresponding to an absorption rate of about $2.8 \times 10^{-3} \text{ dB}/\mu\text{m}$. Therefore, the single-round-trip loss now is

$$A_{\text{Low}} \simeq 2.8 \times 10^{-3} \text{ dB}/\mu\text{m} \cdot L_{\text{Graphene}} + 1.4 \times 10^{-3} \text{ dB}/\mu\text{m} (L_{\text{Ring}} - L_{\text{Graphene}}) \simeq 0.058 \text{ dB} \quad (7)$$

In linear scale, this would account to $\alpha = 0.987$. Inserting this value into Eq. (2) with $t = \alpha_{\text{crit}} = 0.73$ one get $T = 0.84$: at the frequency of resonance the transmission loss is expected to be limited to about 0.75 dB.

When we run the numerical simulation of this case we found that the above prediction was matched almost perfectly. Indeed, we observed that:

- the frequency of resonance changed by about 10 GHz with respect to the graphene's high-conductivity case. This in turn confirms that graphene's conductivity has a very minor effect on the phase constant of the mode;
- at resonance, the “dip” in the transmission curve was equal to 0.48 dB for the low-conductivity case. This curve is shown in the left panel of Fig. 5 with a dashed line. We acknowledge that neither the frequency of resonance nor the depth of the dip are easily inspected in the figure due to the large scale we used. Nevertheless, we preferred to keep both the transmission curves on the same plot as this allows to verify that the proposed device might indeed be regarded as a spectacular optical modulator. The two transmission curves are those of an almost ideal device: a large absorption in the “OFF” state, along with a very reduced insertion loss in the “ON” state, over a remarkably large bandwidth. For instance, if a 6 dB contrast ratio is looked for, a bandwidth as large as 119 GHz would be obtained.

We repeated the same analysis for all the gap values between 80 and 160 nm (at steps of 10 nm). The available 6 dB bandwidth that we computed numerically is shown in the right

panel of Fig. 5 as a function of the gap distance g . In all the cases, the insertion losses we measured never exceeded the level of 0.5 dB.

5. An estimate of the energy required for switch

Graphene's conductivity can be changed by adding (or removing) electrical charges on it. This can be done by realizing a capacitor in which one or both the armatures are formed by graphene layers. Liu et coauthors have shown experimentally both the configurations (see Fig. 1 of ref. [20] and Fig. 1 of ref. [21] for the single and double layer configurations, respectively). Also, they suggested that the double-layer configuration is the best one, as this allows to avoid use of lossy doped silicon to form one of the electrical contacts. In addition, the presence of two graphene layers doubles the effects of the graphene itself.

Observe in our case that lower values of graphene's conductivity are obtained when the charge concentration is raised (see Fig. 3). Also observe in the left panel of Fig. 5 that low graphene's conductivity brings the modulator to its "ON" (i.e. transmitting) state. The reverse applies by lowering the charge concentration. This explains the choice of subscripts we made below Eq. (5).

The structure we have used in our simulations follows Liu's suggestion: two sheets of graphene sandwich a layer of alumina and form the capacitor (see paragraph 2.1). Estimate of the energy required for switching is a trivial application of the capacitor paradox problem. For a pseudo-random bit-sequence this yields

$$E_{\text{PRBS}} = \frac{1}{2} \frac{Q_{\text{ON}}^2 - Q_{\text{OFF}}^2}{2C}$$

The $1/2$ factor accounts for the fact that in a random sequence, switch from bit "0" to bit "1" (or viceversa) only happens one half of the times. The amount of charge required to bring the modulator to the "ON" state is

$$Q_{\text{ON}} = \rho_{\text{ON}} e S \quad , \quad S = \psi_{\text{Graphene}} R_{\text{Ave}} W$$

with e the electron charge and S the extension of the area covered with graphene with R_{Ave} the ring average radius, and W the ring waveguide width, respectively. An analogous expression holds for the "OFF" state too. Neglecting fringing effects, the capacitance of the graphene-alumina-graphene structure is

$$C = \epsilon_0 \epsilon_{\text{rel,diel}} \frac{S}{h_{\text{diel}}}$$

with $\epsilon_{\text{rel,diel}}$ and h_{diel} the relative dielectric constant and thickness of the dielectric oxide between the graphene sheets respectively. The voltage required for charging is

$$V_{\text{ON,OFF}} = \frac{Q_{\text{ON,OFF}}}{C} = \frac{\rho_{\text{ON,OFF}} e}{\epsilon_0 \epsilon_{\text{rel,diel}}} h_{\text{diel}} \quad (8)$$

and the energy required for switching

$$E_{\text{PRBS}} = \frac{1}{2} (\rho_{\text{ON}}^2 - \rho_{\text{OFF}}^2) e^2 \frac{h_{\text{diel}} S}{2\epsilon_0 \epsilon_{\text{rel,diel}}} \quad (9)$$

Some interesting relationships in Eq. (9) are worth of mention:

- *Graphene's surface S .* The charging voltage is independent on S . Whereas, the switching energy linearly scales with it. In this respect, the present configuration might turn out to be advantageous with respect to those of refs. [20, 21] because of the reduced amount of graphene we needed to use here.

- *Oxide's thickness* h_{diel} . Both the voltage and the energy scale linearly with it.
- *Oxide's dielectric constant* $\epsilon_{\text{rel,diel}}$. Both the voltage and the energy scale inversely with it.

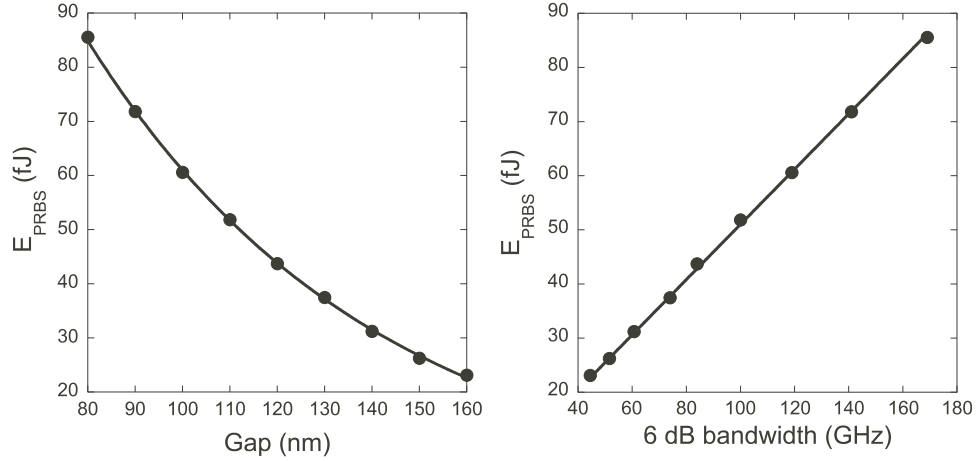


Fig. 6. Left panel: Estimate of the energy required for switching with a pseudo-random bit-sequence (PRBS) in a ring modulator with oxide being constituted by a 7 nm thick layer of alumina ($\epsilon_{\text{rel,diel}} = 10$ at microwaves). Right panel: numerically evaluated dependence of the required switching energy versus the available bandwidth.

A plot of Eq. (9) for oxide being constituted by a 7 nm thick layer of alumina ($\epsilon_{\text{rel,diel}} = 10$ at microwave frequencies) is shown in Fig. 6. Also shown in the figure is the dependence of the energy required for switching as a function of the available bandwidth. A nice linear fit is found, with a pace of about 5 fJ for each 10 GHz increase of the bandwidth.

It is also observed that energies below the level of 100 fJ/bit are estimated for all the values of gap. In addition, from Eq. (8), it is also found that voltages equal to 0.9 and 2.6V would be needed to drive the modulator to the OFF and ON states, respectively. However, it is remarked that, according to the parameters' list of dependencies we have listed above, these values could be further reduced if an oxide layer with either thinner dimensions or higher refractive index were used. For instance, if a 3 nm thick oxide were realized, the energy required for switching would drop to the range of 10÷30 fJ/bit, the pace of growth with bandwidth extension would be reduced to about 2 fJ for additional 10 GHz and, most important, the voltages needed to drive the modulator would fall below 1.2 V, i.e. it would become compatible with state of the art low-voltage CMOS requirements.

A rough estimate of heating effects can also be made. To this end, we first notice that graphene has been proved to be an excellent thermal conductor [30], while the silica cladding which surrounds the whole structure is a thermal insulator. As a consequence, any heating due to dissipation in the graphene layers is transferred very efficiently to the silicon core, which eventually acts as a sort of heat sink for the whole structure.

In the OFF state of the modulator, the light injected in the ring is absorbed by graphene. In order to estimate the change of temperature due to this absorption, we start from the experimental results reported by DeRose and coauthors in ref. [31]. They have shown that the response of a silicon microring can be tuned thermally by dissipating electrical power. The rate of tuning is in the order of 4.4 $\mu\text{W}/\text{GHz}$. Hence, if the ring is fed with a 1 mW continuous-wave laser light, and since this light is absorbed by graphene only for one half of the time, a shift in the

the resonant frequency in the order of 125 GHz may be expected when comparing operations in the “cold” and “heated” graphene cases. Remark that this is a *thermal effect*. That is, the frequency shift can not and does not follow the modulation repetition rate, and only depends on the average level of dissipated power. The frequency of operation of the modulator sets at a steady value after initial thermalization has been completed.

Physically, the 125 GHz shift of the resonant frequency is due to a change of silicon refractive index. One may assume that

$$\frac{\Delta n_{\text{Si}}}{n_{\text{Si}}} \simeq \frac{\Delta f}{f} \rightarrow \Delta n_{\text{Si}} \simeq \frac{0.125 \text{ THz}}{200 \text{ THz}} \sqrt{12} \simeq 2 \times 10^{-3}.$$

Since the thermo-optic coefficient of silicon is in the order of $2 \times 10^{-4} \text{ K}^{-1}$, a temperature change in the order of ten degrees is therefore expected in silicon (and graphene) when operating the modulator. With respect to room temperatures, this represent less than a 5% change, so that the effect on both the Fermi–Dirac distribution and the complex conductivity of graphene is expected to be rather modest. Presence of cooling devices outside the modulator might further decrease this effect.

6. Conclusion

We have proposed a novel device which exploits controllability of graphene’s optical conductivity to realize a critically-coupled ring-modulator based on the physical mechanism first introduced by Yariv in ref. [1]. The modulator is designed to be at the critical condition for high graphene’s conductivity. In this state, no light is transmitted from the input to the output port. Whereas, when graphene’s conductivity is switched to its low state, propagation in the ring becomes almost lossless, and a dramatic increase of the transmitted power is observed.

Notice that we deliberately added losses to the propagation in the ring through insertion of graphene. This way, the overall Q-factor of the ring turned out to be rather low and no sharp resonances were formed. This is the major difference with respect to ring modulators based on the plasma–dispersion–induced effect. Indeed, in those modulators, ON–OFF switching is obtained by changing the refractive index in the ring, causing this way a detune of the frequency of resonance. However, since the change of refractive index one may reasonably obtain is small, a sharp transmission resonance is needed in order to realize a respectable contrast ratio. Typical values of bandwidth that can be obtained in this way are in the order of 10–20 GHz. On the contrary, our design does not rely on frequency detuning. This in turn means that it may work with broad resonances too, as we proved with the help of numerical simulations. Bandwidths in the range of 100 GHz were found, though larger ones might actually be obtained if gap smaller than 100 nm could be manufactured.

Observe that a bandwidth in the order of 100 GHz is not merely a valuable figure of merit because of the transmission rates this modulator could work at. Actually, such a large bandwidth could allow to get rid of temperature control circuits that are usually needed to lock a sharp resonance to the right wavelength. Keeping in mind that the power consumption of these control circuits greatly exceeds those of the modulators themselves, the present device could eventually lead to a dramatic reduction of the energy required for switching which, in our case, could really approach the level of few fJ per bit.